Inorganic Chemistry

ARTICLE

pubs.acs.org/IC

Visualizing Diastereomeric Interactions of Chiral Amine−Chiral Copper Salen Adducts by EPR Spectroscopy and DFT

Damien M. Murphy,*[,†] Ignacio Caretti,[‡] Emma Carter,[†] Ian A. Fallis,*[,†] Marcus C. Göbel,[†] James Landon,[†] Sabine Van Doorslaer,*[,‡] and David J. Willock[†]

[†]School of Chemistry, Cardiff University, Main Building, Park Place, Cardiff CF10 3AT, United Kingdom

[‡]SIBAC Laboratory, Department of Physics, University of Antwerp, Universiteitsplein 1, B-2610 Wilrijk, Belgium

Supporting Information

ABSTRACT: Single enantiomers of *R*/*S*-methylbenzylamine (MBA) were found to selectively form adducts with two chiral Cu−salen complexes, [Cu^{II}(**1**)] (H_2**1** = *N*,*N*′-bis(3,5-ditert-butylsalicylidene)-1,2-diaminocyclohexane) and [Cu^{II}(**2**)] (H_2**2** = *N*,*N*′-bis-salicylidene-1,2-cyclohexanediamino). The axial *g*/*A* spin Hamiltonian parameters of the Cu−MBA adducts were typical of 5-coordinate species. Enantiomer discrimination in the MBA binding was directly evidenced by W-band CW EPR, revealing an 86 ± 5% preference for formation of the *R*,*R*-[Cu(**1**)] + *S*-MBA adducts compared to *R*,*R*-[Cu(**1**)] + *R*-MBA; this was reduced to a 57 ± 5% preference for *R*,*R*-[Cu(**2**)] + *S*-MBA following removal of the *tert*-butyl groups. The structure of these diastereomeric adducts was further probed by different hyperfine techniques (ENDOR and HYSCORE), although no structural differences were detected between these adducts using these techniques. The diastereomeric adducts were found to possess lower symmetry, as evidenced by rhombic ***g*** tensors and inequivalent H^{imine} couplings. This was caused by the selective binding mode of MBA onto one side of the chiral Cu^{II} complex. DFT calculations were performed on the *R*,*R*-[Cu(**1**)] + *S*-MBA and *R*,*R*-[Cu(**1**)] + *R*-MBA adducts. A distinct difference in orientation and binding mode of the MBA was identified in both adducts, confirming the experimental results. The preferred heterochiral *R*,*R*-[Cu(**1**)] + *S*-MBA adduct was found to be 5 kJ mol^{-1} lower in energy compared to the homochiral adduct. A delicate balance of steric repulsion between the α-proton (attached to the asymmetric carbon atom) of MBA and the methine proton (attached to the asymmetric carbon atom) of [Cu(**1**)] was crucial in the stereoselective binding.

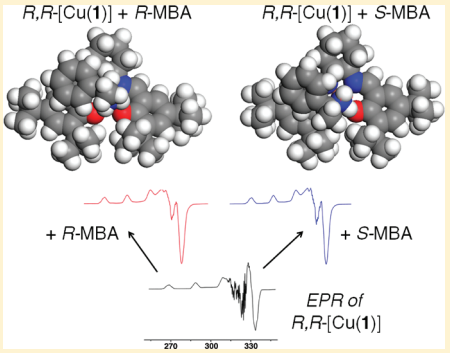

INTRODUCTION

In recent years transition-metal complexes have been extensively used in asymmetric catalytic transformations of racemic, prochiral, and optical substrates to yield single-enantiomer compounds.[1] The importance of this field was recognized 10 years ago, when Knowles, Noyori, and Sharpless received the Nobel Prize in chemistry for their work on chirally catalyzed hydrogenation/oxidation reactions.[2] To optimize efficiency, these catalysts should strictly differentiate enantiotopic groups or faces of prochiral molecules.[3] Optimization can be modulated based on the choice of metal (Cu, Mn, Co, Fe, Cr, etc.) or the choice of chiral organic ligands coordinated to the metal center. Ligands with central chirality, axial chirality, and planar chirality can thus be easily tailored in order to fine tune the desired enantioselectivities.[4]

One very versatile class of organic ligand for homogeneous asymmetric catalysis is the salen ligand [1,6-bis(2-hydroxyphenyl)-2,5-diazahexa-1,5-diene].[5] Much of this versatility originates from the structural rigidity of the ligand,[6] which is reminiscent of the porphyrin framework in heme-based oxidative enzymes;[7] the ligand can thus easily stabilize metal ions in an asymmetric environment yet is easy to synthesize and derivatize relative to porphyrins.[8] Early pioneering work on these ligands for asymmetric catalysis was performed by Jacobsen and Katsuki.[5,9] Chromium and cobalt complexes of the same *N*,*N*′-bis(3,5-di-*tert*-butylsalicylidene)-1,2-cyclohexanediamino ligand (**1**) (Scheme 1) were also found to catalyze the highly enantioselective ring-opening reactions of epoxides.[10]

Despite the phenomenal success of these catalysts, a great deal of research has been devoted to understanding their mode of operation. This is particularly true for the epoxidation reaction, where many key aspects of the reaction are still not fully understood (i.e., nature of oxygen-transferring species, mechanism of the oxygen transfer step, nature of highly efficient stereochemical communication between catalyst and substrate).[7] Several approaches, including computational and spectroscopic methods, have been applied to explore how the steric properties of the ligand contribute to the asymmetric chiral induction mechanism and to verify the precise transition state of the asymmetric reaction.[11]

One very versatile but often under exploited spectroscopic tool for studying homogeneous catalytic reactions is electron paramagnetic resonance (EPR) and the related hyperfine

Received: January 18, 2011
Published: June 27, 2011

Scheme 1. Structure of the *N,N′*-Bis(3,5-di-*tert*-butylsalicylidene)-1,2-cyclohexanediamino Metal Complex, *N,N′*-Bis-(3,5-di-*tert*-butylsalicylidene)-1,2-cyclohexanediamino Copper(II) ([Cu(1)], and the *N,N′*-Bis-salicylidene-1,2-cyclohexanediamino Copper(II) ([Cu(2)]) complex[a]

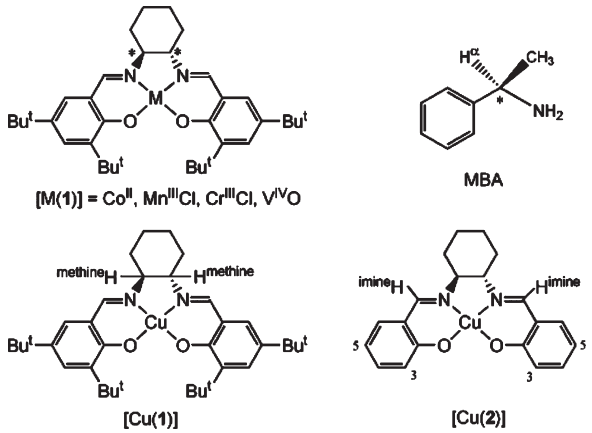

[a] The structure of the chiral methylbenzylamine (MBA) is also shown. Chiral centers are labeled with an asterisk (*).

techniques of ENDOR (electron nuclear double resonance), ESEEM (electron spin echo envelope modulation), and HYSCORE (hyperfine sublevel correlation) spectroscopy.[12,13] For example, in the specific case of metal−salen-based catalysts, active Mn^{V}=O species in the [MnCl(**1**)] complex have been investigated by EPR.[14−17] The Cr spin states in [CrCl(**1**)], of relevance to catalytic epoxidation, have also been studied.[18] Recently, we investigated the electronic structure of acetic-acid-activated [Co(**1**)], of relevance to hydrolytic kinetic resolution,[19] and identified an unusual coordinated phenoxyl radical, $[Co^{III}(\mathbf{1}^{\bullet})(OAc)_n](OAc)_m$, among several paramagnetic centers in the activated catalyst.[19]

In most of these investigations, the emphasis of the work was devoted to the electronic properties of the central metal[15−18] or ligand.[19] However, as reported by Movassaghi and Jacobsen,[20] homogeneous asymmetric metal catalysts can behave like enzymes by exploiting hydrogen bonding between the active site and substrate together with nonbonded dipole−dipole, electrostatic, and steric interactions to orient the substrate and stabilize the transition state, leading to high levels of stereoselectivity. We have already shown how some of these weak outer-sphere forces can be studied by EPR, ENDOR, HYSCORE, and DFT in the related chiral [VO(**1**)] undergoing interaction with chiral epoxides; in particular, we showed how weak electrostatic forces, steric interactions, and H bonds affect the manner in which the chiral epoxides bind to the chiral [VO(**1**)] complexes.[21]

In this work, we will examine how the asymmetric copper complexes [Cu(**1**,**2**)] (Scheme 1) can differentiate and discriminate between single enantiomers of a chiral amine (*R*- and *S*-methylbenzylamine). Our choice of chiral ligands **1** and **2** was motivated by a desire to establish the possible role of $\pi-\pi$ interactions, H bonds, or simple steric repulsion in controlling the outcome of these diastereomeric interactions. For example, it is well known that $\pi-\pi$ interactions control the conformational preferences and binding in macrocycles, complexation in many host−guest systems, porphyrin aggregation, and the structure of DNA.[22] It is not clear if these and other weak forces control the mode of stereoselective binding in asymmetric metal complexes with organic substrates bearing phenyl groups. While advanced EPR techniques have been widely used to examine the nature of the copper binding sites in various proteins, metalloenzymes,[23] or even relatively simple organometallic complexes,[24] they have not been widely employed to study asymmetric complexes of relevance to catalysis. In this work we will show how high-frequency EPR can be used to examine the binding site in an asymmetric metal complex bearing a coordinated asymmetric substrate. Using W-band EPR, we will show the extent of enantiodiscrimintaion in [Cu(**1**)] versus [Cu(**2**)]. ENDOR and HYSCORE have also been used to investigate the structure of the adducts, although in this case these techniques were unable to detect any differences between the diastereomeric adducts. The origins of this diastereoselective binding is explained by DFT.

EXPERIMENTAL SECTION

Synthesis. All reagents and solvents (Aldrich) were used as received. Ligands H_2**1** and H_2**2** were prepared as described previously.[20] Complexes [Cu(**1**)] and [Cu(**2**)] (Scheme 1) were prepared by the methods of Bunce et al.[25a] and Bernado et al.,[25b] respectively. Complexes were purified by filtration through a short pad of silica to afford chromatographically homogeneous samples. d_2-MBA was prepared by washing a CH_2Cl_2 (50 mL) solution of MBA (5 g) with several portions of D_2O (3 × 30 mL). The organic layer was dried ($MgSO_4$), and the solvent was removed in vacuo. The residue was distilled to afford d_2-MBA in quantitative yield. The degree of deuteration was estimated to be ∼90% (analysis by electrospray mass spectrometry).

X-Band Pulsed EPR. The X-band pulsed EPR and pulsed ENDOR experiments were performed with an ELEXSYS Bruker spectrometer (mw frequency 9.73 GHz) equipped with a liquid-helium cryostat from Oxford Inc. All experiments were recorded at 10 K with a repetition rate of 1kHz. The magnetic field was measured with a Bruker ER035 M NMR Gaussmeter. HYSCORE experiments[27] were carried out using the pulse sequence $\pi/2-\tau-\pi/2-t_1-\pi-t_2-\pi/2-\tau-$echo, with pulse lengths of $t_{\pi/2} = t_{\pi} = 16$ ns. Times t_1 and t_2 were varied from 96 to 5680 ns in steps of 16 ns. An eight-step phase cycle was used to eliminate unwanted echoes. The individual time traces were baseline corrected with a third-order polynomial, apodized with a Hamming window, and zero filled. After 2D Fourier transformation, the absolute-value spectrum was calculated. The HYSCORE spectra were simulated using a GAMMA-based program developed at the ETH Zurich.[28] The same sets of τ values as in the experiments were taken. Davies-ENDOR experiments[29] were carried out using the following pulse sequence: $\pi-T-\pi/2-\tau-\pi-\tau-$echo. The experiments were done with mw pulse lengths of $t_{\pi} = 256$ ns, $t_{\pi/2} = 128$ ns, and an interpulse time τ of 800 ns. An rf τ pulse of variable frequency and a length of 18 μs was applied during time T of 20 μs.

W-Band CW and Pulsed EPR. The W-band EPR measurements were performed on a Bruker Elexsys E680 spectrometer equipped with a continuous gas-flow cryostat (Oxford Instruments). The spectra were recorded using microwaves of ∼94 GHz frequency and 0.044 mW power at a fixed temperature of 100 K. The magnetic field was swept in the 2950−3350 mT range with a modulation frequency and amplitude of 100 kHz and 0.5mT, respectively. The W-band ELDOR (electron−electron double resonance)-detected NMR experiments[30] were performed using the pulse sequence $(HTA)_{mw2}-t_1-(\pi/2)_{mw1}-\tau-(\pi)_{mw1}-\tau-$echo with $(\pi/2)_{mw1}$ and $(\pi)_{mw1}$ pulses of 220 and 440 ns, a 50 μs high-turning angle $(HTA)_{mx2}$ pulse with mw frequency 2, and interpulse delay times t_1= 1 μs and τ_2 = 2 μs. The experiments were performed at 5 K with a repetition rate of 667 Hz.

dx.doi.org/10.1021/ic200113u |*Inorg. Chem.* 2011, 50, 6944–6955

Computational Details. The interaction of *R*- and *S*-MBA with *R,R*-[Cu(**1**)] was studied computationally using a mixed quantum mechanics/molecular mechanics (QMMM) approach through the ONIOM method[31] within the Gaussian03 package.[32] The metal complex including the metal center, phenyl, and methine groups along with the MBA were treated at the QM (BHandH) level, while the remaining aliphatic *tert*-butyl groups and cyclohexyl backbone were studied at the MM level (universal force field, UFF).[33] This division of the atoms is illustrated in the Supporting Information (Figure S13) and is chosen to ensure that the boundary region consists of only σ bonds. Hydrogen link atoms are used to satisfy the valency of the QM region at this interface.

One aspect of the MBA interaction with [Cu(**1**)] is the presence of aromatic groups in both species. Selection of BHandH was based on recent work comparing a range of functionals for describing benzene, pyridine, and DNA base dimers.[34] This clearly shows that minima on the potential energy surfaces with the BHandH functional give qualitative agreement with MP2 structures and can reproduce interaction energies generally to within ± 2 kJ mol^{-1}. BHandH is a hybrid functional with the exchange component of the electron−electron interaction represented using one-half Hartree−Fock and one-half local spin density approaches. The correlation energy is drawn from the functional due to Lee, Yang, and Parr.[35] Within the QM region we also employ the LANL2DZ effective core potential (ECP) and related basis set for Cu, the 6-31G(d,p) basis for C, O, and H, and 6-31+G(d,p) for N. The additional diffuse function at N was introduced to improve the description of the MBA−[Cu(**1**)] interaction involving the coordinating nitrogen atom.

In order to compute the EPR parameters, spin-unrestricted density functional computations were performed with the ORCA package[36] on the two most stable geometries of *R,R*-[Cu(**1**)] + *S*-MBA and the single most stable geometry of *R,R*-[Cu(**1**)] + *R*-MBA. The computations were performed with the B3LYP functional. For calculation of the EPR parameters, basis sets with significant flexibility in the core region were used, i.e., the ORCA basis sets CoreProp (CP(III))[37] was used for copper, and a Barone basis set 'EPRII'[38] was taken for the nitrogen and hydrogen atoms. For the other atoms, a split-valence plus polarization (SV(P)) basis set was assumed.[39] The solvent surrounding was simulated by assuming a dielectric surrounding with the dielectric constant of MBA (ε = 4.4 at 18 °C) using the conductor-like screening model (COSMO).[40]

RESULTS

The chiral amines (*R*- and *S*-MBA) and chiral copper complexes (*R,R*- and *S,S*-[Cu(**1,2**)] can form four different 5-coordinate diastereomeric adducts; namely, *R,R*-[Cu(**1,2**)] + *R*-MBA, *R,R*-[Cu(**1,2**)] + *S*-MBA, *S,S*-[Cu(**1,2**)] + *R*-MBA, and *S,S*-[Cu(**1,2**)] + *S*-MBA (abbreviated hereafter to *RR-R*, *RR-S*, *SS-R*, and *SS-S*, see Scheme S1, Supporting Information). The assumption that only 5-coordinate Cu(II) adducts are formed was verified in various dilution experiments (see later). Since the two adducts *RR-R* and *SS-S* are enantiomers of each other and will have the same structure and stability, they are henceforth referred to as the "homochiral" pairs or adducts. Similarly, the adducts *RR-S* and *SS-R* are enantiomers and will be referred to as the "heterochiral" pairs or adducts. The homochiral and heterochiral pairs of enantiomers are diastereomers and have different structures, stabilities, and spectroscopic properties. X- and W-band CW EPR spectra were therefore recorded for different combinations of the copper complexes and chiral amines to test which adducts are preferentially formed. This involved first measuring the EPR spectra of the individual homochiral combinations (i.e., *RR* dissolved in *R*-MBA and *SS* dissolved in *S*-MBA) and heterochiral combinations (i.e., *RR* in *S*-MBA and *SS* in *R*-MBA). The preferential formation of one adduct over another was further confirmed in separate competitive experiments, whereby either *rac*-[Cu(**1,2**)] was dissolved in *rac*-MBA (denoted as a '*rac-rac*' combination) or alternatively one enantiomer of [Cu(**1,2**)] was dissolved in *rac*-MBA (denoted *RR-rac* or *SS-rac* combinations).

CW-EPR SPECTRA (X BAND)

The X-band CW-EPR spectra for [Cu(**1**)] dissolved in MBA are shown in Figure 1b−f together with the parent spectrum of *rac*-[Cu(**1**)] dissolved in toluene (Figure 1a). Figure 1b shows the EPR spectrum of the competitive *rac-rac* combination, Figure 1c and 1d shows the spectra of the heterochiral pairs, while Figure 1e and 1f shows the homochiral pairs. The equivalent series of spectra for [Cu(**2**)] are shown in the Supporting Information (Figure S1).

The EPR spectra of [Cu(**1**)] and [Cu(**2**)] measured in toluene (i.e., in the absence of amine) display axial ***g*** and copper hyperfine ($\boldsymbol{A}^{Cu}$) tensors. This was confirmed at W-band frequencies (Figures 2d and 3d). Further superhyperfine splittings are also readily observed at X-band (Figure 1) due to the strong interaction of the unpaired electron with the two equivalent nitrogen nuclei and two equivalent imine protons of the Schiff-base ligand (Scheme 1). These proton and nitrogen superhyperfine splittings are expected for 4-coordinate Cu(II) complexes.[41] The spin Hamiltonian parameters obtained from the simulated EPR spectra are listed in Table 1. These parameters are in good agreement with those obtained from a single-crystal EPR study of the closely related [Cu(salen)] complex.[42] EPR spectra for frozen solutions of [Cu(**1**)] were also recently reported within the context of galactose oxidase-inspired complexes.[43]

The individual spectra of [Cu(**1**)] in MBA are shown in Figure 1b−f and are obviously different compared to Figure 1a (of [Cu(**1**)] in toluene); this is indicative of amine binding to the copper complex. The most notable changes are the increasing $g_{||}$ and decreasing $A_{||}$ values; these trends are consistent with the weak axial coordination of a fifth ligand (MBA) to the poorly Lewis acidic [Cu(**1**)]. The resolution of the superhyperfine splittings in the $g = g_{\perp}$ region is substantially reduced compared to the spectrum observed in the absence of amine (Figure 1a). This loss of resolution is largely due to the subtle changes in the ^{1}H and ^{14}N hyperfine couplings arising from the redistribution of spin density on the nitrogen and imine protons, which generally accompanies the axial coordination of a fifth ligand to copper centers.[41] The loss in superhyperfine resolution is even more pronounced for the [Cu(**2**)] complex (Supporting Information; Figure S1). This suggests that MBA is weakly coordinated to [Cu(**1,2**)] but does not reveal the number of bound MBA molecules.

To answer this question, a series of dilution measurements was performed in which the Cu:MBA ratios were systematically varied from 1 to 20 for a constant concentration of [Cu(**1**)] or [Cu(**2**)]; these spectra were compared to the two limiting situations of [Cu(**1,2**)] recorded in neat toluene/dichloromethane or in excess MBA. The resulting spectra could be treated as a linear combination of the individual spectra observed in the presence and absence of MBA (see Supporting Information; Figure S2), and thus, it was possible to determine the number of coordinated MBA molecules. For both complexes, this revealed that only one bulky MBA molecule was bound to the bulky Cu complex. This is

dx.doi.org/10.1021/ic200113u |*Inorg. Chem.* 2011, 50, 6944–6955

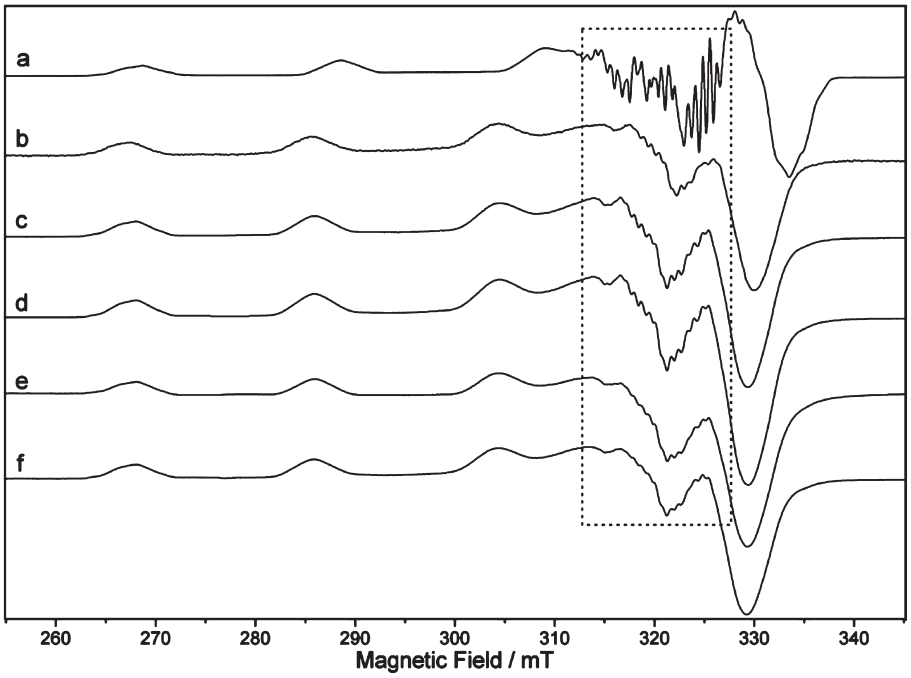

Figure 1. X-band CW EPR spectra (recorded at 140K) of (a) the noncoordinated [Cu(**1**)] complex dissolved in toluene together with the different [Cu(**1**)] + MBA combinations of (b) *rac-rac*, (c) *RR-S*, (d) *SS-R*, (e) *RR-R*, and (f) *SS-S*.

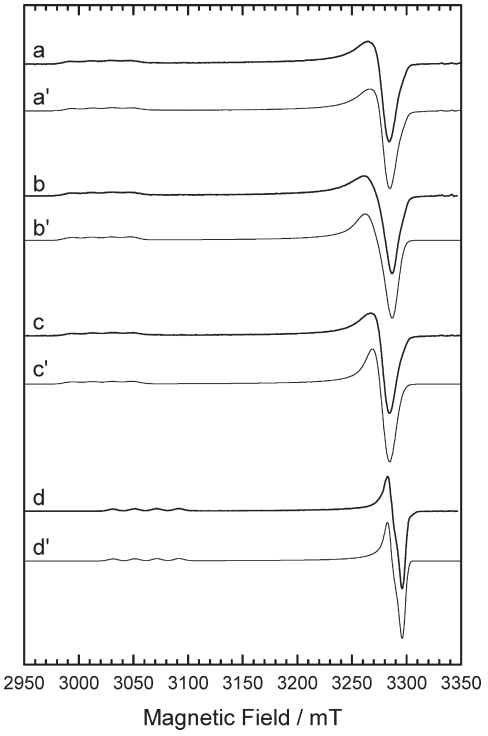

Figure 2. W-band CW EPR spectra (recorded at 100K) of *S,S*-[Cu(**1**)] dissolved in (a) *rac*-MBA, (b) *S*-MBA, (c) *R*-MBA, and (d) toluene. The corresponding simulations (a′, b′, c′, and d′) are plotted below each spectrum; (a′) obtained by addition of experimental spectra c and b in a ratio of 86:14.

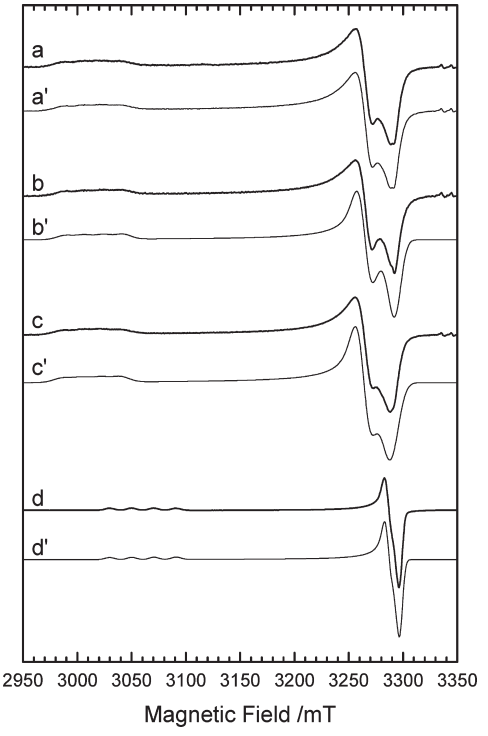

Figure 3. W-band CW EPR spectra (recorded at 100K) of *S,S*-[Cu(**2**)] dissolved in (a) *rac*-MBA, (b) *S*-MBA, (c) *R*-MBA, and (d) DCM. The corresponding simulations (a′, b′, c′, and d′) are plotted below each spectrum; (a′) obtained by addition of experimental spectra c and b in a ratio of 57:43.

not surprising considering the propensity for Cu(II) complexes to form 5 (i.e., 4 + 1) coordinate complexes.

Closer inspection of the spectra in the $g = g_{\perp}$ region reveals some interesting features (Figure 1). The EPR spectra of the

dx.doi.org/10.1021/ic200113u |*Inorg. Chem.* 2011, 50, 6944–6955

Table 1. Experimental and DFT-Computed Principal g and ^{63}Cu Spin Hamiltonian Parameters for *rac*-[Cu(**1**)] and *rac*-[Cu(**2**)] Dissolved in Toluene (tol) and Dichloromethane (dcm)[a]

solvent/matrix	g_3	g_2	g_1	A_3 /MHz	A_2 /MHz	A_1 /MHz
rac-[Cu(**1**)] + tol	2.1937	2.0408	2.0408	−605 ± 10	−90 ± 5	−90 ± 5
rac-[Cu(**2**)] + dcm	2.1957	2.0416	2.0416	−617 ± 10	−90 ± 5	−90 ± 5
[b] *R,R*-[Cu(**1**)] + *R*-MBA	2.2226	2.0475	2.0475	−565 ± 10	−60 ± 10	−60 ± 10
R,R-[Cu(**1**)] + *S*-MBA	2.2235	2.0436	2.0532	−550 ± 10	−60 ± 10	−60 ± 10
R,R-[Cu(**2**)] + *R*-MBA	2.2310	2.0442	2.0600	−535 ± 10	−65 ± 10	−65 ± 10
R,R-[Cu(**2**)] + *S*-MBA	2.2230	2.0428	2.0600	−550 ± 10	−65 ± 10	−65 ± 10

	g_z	g_y	g_x	A_z/MHz	A_y /MHz	A_x /MHz
A	2.1504	2.0532	2.0380	−565.3	−9.5	−72.6
B	2.1492	2.0525	2.0385	−565.3	−6.1	−67.6
C	2.1513	2.0543	2.0375	−563.6	−12.4	−76.7

[a] The DFT-computed principal values correspond to the optimized structures **A** and **B** of the *R,R*-[Cu(**1**)] + *R*-MBA adduct and structure **C** for the *R,R*-[Cu(**1**)] + *S*-MBA adduct (Figure 5). [b] Only the values for *R,R*-[Cu(**1,2**)] + *R/S*-MBA are given, since *S,S*-[Cu(**1,2**)] + *R/S*-MBA gives similar results; $g_1,g_2 = g_\perp$; $g_3 = g_{||}$. $A_1,A_2 = A_\perp$; $A_3 = A_{||}$. $A_\perp$ values obtained from X-band spectra. Error in g values is ±0.0005

heterochiral pairs (Figure 1c and 1d) are identical to each other, as are the homochiral combinations (Figure 1e and 1f). Satisfyingly, a comparison of the heterochiral (Figure 1c and 1d) and homochiral (Figure 1e and 1f) structures reveals differences in the spectra, as expected for a set of diastereomers. Measurement of the *rac-rac* spectrum (Figure 1b) was undertaken to determine the extent, if any, of chiral discrimination in the system. Theoretically, if both homochiral and heterochiral adducts were equally formed in a *rac-rac* solution then, under the magnetically dilute conditions employed, Figure 1b should represent an equal summation of Figure 1c and 1d and Figure 1e and 1f. In fact, Figure 1b is comparatively closer to Figure 1c and 1d compared to Figure 1e and 1f. This important observation suggests that there is a preferential formation of the heterochiral adducts in frozen solution and that [Cu(**1**)] is capable of discriminating enatiomers of MBA.

CW-EPR SPECTRA (W BAND)

The high-field EPR spectra of *S,S*-[Cu(**1**)] dissolved in *rac*-, *R*-, and *S*-MBA are shown in Figure 2a, 2b, and 2c, respectively. Figure 2d corresponds to *S,S*-[Cu(**1**)] dissolved in toluene for comparison. Simulations are depicted below each experimental spectrum and labeled as Figure 2a′−d′. It should be noted that the g-strain effect is 10 times larger at W-band frequencies compared to the X band; as a result, the hyperfine splitting resolution is lost in the $g = g_\perp$ region. The narrower line width of the complex dissolved in toluene (Figure 2d) compared to MBA (Figure 2a−c) points to smaller g and A strain effects in the noncoordinated [Cu(**1**)]−toluene case compared to the [Cu(**1**)]−MBA adducts.

As observed at the X band, the W-band EPR spectra in Figure 2 reveal that amine coordination has a considerable effect on the spin distribution in the copper center. Consequently, the [Cu(**1**)]−MBA adducts show an increase of the g values and a decrease of the copper hyperfine constants (in absolute values) compared to [Cu(**1**)] (Table 1). This variation of $g_{||}$ and $A_{||}$ further confirms axial coordination of the MBA. Examination of the spin Hamiltonian parameters of [Cu(**1**)]−MBA diastereomers in Table 1 reveals a small rhombicity of the $\boldsymbol{g}$ tensor for the homochiral pair (*SS-S*) that could not be detected at X-band frequencies. This deviation of the $\boldsymbol{g}$ tensor from axial symmetry is evidence for a different binding mode of the MBA in the homochiral pair (*SS-S*) than in the heterochiral one (*SS-R*), where axial nature is retained, and indicates a lowering of symmetry at the metal center in the homochiral case. Again, this is evidence for a discrimination of the MBA enantiomers by the [Cu(**1**)] complex. The W-band EPR spectrum of *S,S*-[Cu(**1**)] dissolved in *rac*-MBA (*SS-rac*) is shown in Figure 2a, with a simulation based on an 86:14 contribution of *SS-R*:*SS-S* (using the least-squares method). Therefore, the *S,S*-[Cu(**1**)] complex preferentially binds the *R*-MBA enantiomer with a selectivity of (86 ± 5)% (i.e., favoring the heterochiral pair). These results quantify the earlier qualitative trends observed in the X-band EPR spectra (Figure 1).

A similar set of experiments was also conducted using [Cu(**2**)]. The W-band CW-EPR spectra of *S,S*-[Cu(**2**)] dissolved in *rac*-MBA, *R*-MBA, *S*-MBA, and CH_2Cl_2 (owing to the poor solubility of [Cu(**2**)] in toluene) are shown in Figure 3. Similarly to [Cu(**1**)], [Cu(**2**)] exhibits a square-planar geometry with a g_z value 0.002 larger than in [Cu(**1**)] and where A_3 has increased in absolute value by 10 MHz. The binding of *R*- or *S*-MBA to *S,S*-[Cu(**2**)] now results in a pronounced rhombic distortion (Table 1) as shown by two well-resolved peaks in the perpendicular region. These extra peaks cannot arise from a second Cu(II) center, since no extra peaks are detected in the parallel region, neither at the X band nor at the W band. Spectral simulations for [Cu(**2**)]−MBA adducts revealed that the heterochiral adduct (*SS-R*) is preferred over the homochiral adduct (*SS-S*) but with only a 57:43 contribution of *SS-R*:*SS-S*, indicating that the heterochiral pair is only slightly favored at 57(±5)%. This key observation indicates a poorer discrimination of enatiomers of MBA by [Cu(**2**)] compared to that of [Cu(**1**)].

ENDOR AND HYSCORE SPECTRA

To probe the structure of the diastereomeric MBA adducts further, ENDOR and HYSCORE were used to examine the ^{1}H and ^{14}N couplings from the ligand and coordinated MBA molecule ($-NH_2$). Although relevant changes in the hyperfine parameters of the ligand nuclei can be detected by ENDOR and HYSCORE, no significant difference between the diastereomeric adducts could be revealed using these hyperfine techniques. A summary of the key findings from these hyperfine techniques is thus presented below.

dx.doi.org/10.1021/ic200113u |*Inorg. Chem.* 2011, 50, 6944–6955

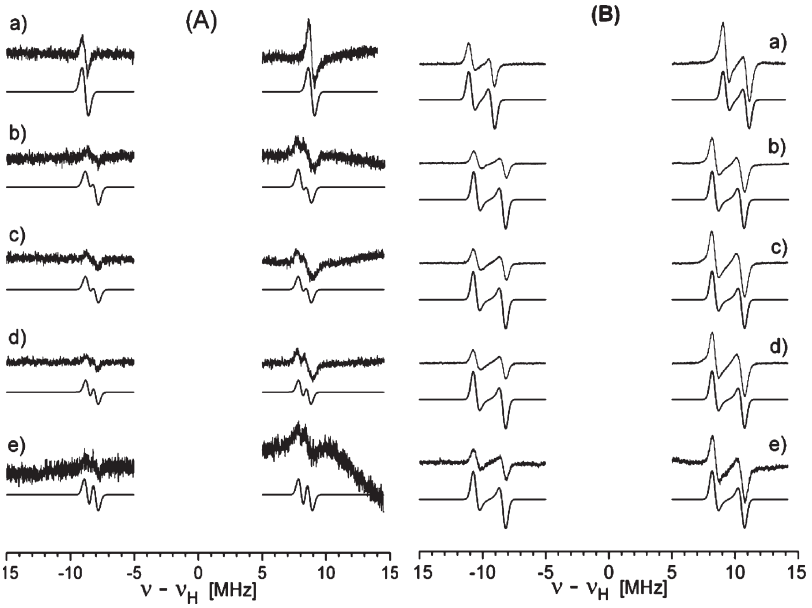

Figure 4. Q-band ^{1}H CW ENDOR spectra (recorded at 10K) showing the H^{imine} couplings of (a) *rac*-[Cu(**2**)] dissolved in d^8-toluene/d^6-dichloromethane and (b) *SS-R*, (c) *RR-S*, (d) *SS-S*, and (e) *RR-R*. Spectra recorded at (A) $g = g_\parallel = g_3$ and (B) $g = g_\perp = (g_1 + g_2)/2$. For clarity, the central part of the spectra, containing proton couplings from the remaining ligand nuclei and coordinated MBA, have been removed.

The Q-band ENDOR spectra of [Cu(**2**)] recorded at field positions corresponding to $g = g_\perp$ and $g = g_3 = g_\parallel$ are shown in Figure 4. The corresponding hyperfine values extracted from the simulations are given in Table 2. The analogous series of spectra for [Cu(**1**)] are shown in the Supporting Information (Figure S5). In the absence of MBA, the two imine protons appear equivalent for both [Cu(**1**)] and [Cu(**2**)]. This equivalency can be clearly seen in Figure 4a for the spectrum measured at $g = g_\parallel$, where only one pair of lines is observed. The a_{iso} values and Cu−H^{imine} distances of 3.8 Å (estimated from A_{Dip} using a simple point-dipole approximation) are in very good agreement with the single crystal of [Cu(**1,2**)][25a,b] and the structurally related [Cu(salen)] complex.[42]

Upon addition of MBA, the equivalency of the imine protons is removed. The spectra of the homochiral (*RR-R*, *SS-S*) and heterochiral (*RR-S*, *SS-R*) adducts are given in Figure 4b−e; two distinct differences can now be observed. First, a small decrease in the magnitude of a_{iso} accompanies MBA coordination to [Cu(**1**)] and [Cu(**2**)] (see Supporting Information; Table S1). A decrease of a_{iso} was also reported for the imine protons upon axial coordination of a fifth ligand (pyridine) to [Cu(salen)],[42] caused by a lowering of covalency in the complex. Second, the equivalency of the two imine protons is removed upon MBA binding and two distinct protons (labeled H_A and H_B) can now be distinguished (Table 2). Again, this inequivalency can be seen in Figure 4b−e for the spectra measured at $g = g_\parallel$; two pairs of lines are now clearly visible centered on ν_H. This inequivalency in the ligand imine protons is due to a lowering in the symmetry of the [Cu(**2**)] + MBA adduct, compared to the parent [Cu(**2**)] complex. These results support the earlier direct findings by W-band EPR, whereby a rhombic distortion was found for the [Cu(**2**)] + MBA adduct (Figure 3), indicative of a lower symmetry.

In the [Cu(**1**)] + MBA adduct, the inequivalency in the imine protons was barely perceptible, manifested only by a broadening of the proton peaks in the ENDOR simulations, rather than a complete splitting of the peaks (Supporting Information; Figure S5). Again, these results support the earlier W-band data, whereby the rhombic distortion in the [Cu(**1**)] + MBA adduct (Figure 2) was almost negligible compared to [Cu(**2**)] (Figure 3). We next examined the couplings to the ligand methine protons in [Cu(**1,2**)] and *tert*-butyl protons in [Cu(**1**)] by CW and Davies ENDOR (experimental and simulated spectra shown in the Supporting Information; Figures S6−S8). The hyperfine couplings (hfc) for these two sets of protons are given in Table 2. It should be clearly noted that these hyperfine couplings did not alter dramatically in the presence or absence of MBA. This suggests little interaction between the bound MBA and these protons nor any substantial distortions of the [Cu(**1,2**)] ligand framework. We also examined the ENDOR spectra arising from the amine protons ($-NH_2$) of the coordinated MBA (Supporting Information; Figures S9−S10). The assignment of the peaks due to the $-NH_2$ group was confirmed by comparison of the ENDOR spectra recorded for [Cu(**1,2**)] in the absence of MBA with those recorded using MBA and d_2-MBA (Supporting Information; Figures S11). The simulated hyperfine couplings for the amine protons are listed in Table 2. These values are expected for a weakly coordinated amine. Despite recording the ENDOR spectra of the amine protons for a set of diastereomeric adducts (*RR* + *S* versus *RR* + *S*), we could not detect any significant differences.

Q-band ^{14}N ENDOR spectra of [Cu(**1,2**)] in toluene and MBA were also measured (Supporting Information; experimental and simulated Q-band CW spectra shown in Figures S12 and S13 and X-band Davies ENDOR is shown in Figure S8). For the parent complexes dissolved in toluene/dichloromethane, both the hfc and the nuclear quadrupole tensors of the two nitrogen nuclei were found to deviate slightly from axial symmetry; their largest principal axes were approximately directed to the copper ion. The simulated parameters (Table 3) are very similar to those reported for [Cu(salen)].[42]

Upon coordination of MBA, a reduction in the ^{14}N hfc is observed for both [Cu(**1,2**)] and is analogous with the earlier

dx.doi.org/10.1021/ic200113u |*Inorg. Chem.* 2011, 50, 6944–6955

observation of a reduction in a_{iso} for the imine protons (Figure 4); this is again consistent with axial coordination of MBA. A noted decrease in the asymmetry parameter η of the bound adduct can also be observed for [Cu(**2**)], while it is less pronounced for [Cu(**1**)]. The ^{14}N ENDOR spectra were also notably broader (and less intense) for the [Cu(**1**,**2**)]-MBA adducts compared to the parent complexes (Supporting Information; Figures S12 and S13). While solvation issues cannot be ignored completely (i.e., MBA vs toluene/DCM), this broadening of the lines may arise from an inequivalency of the two ligand nitrogen nuclei in the adducts. These observations corroborate the inequivalency observed above for the imine protons.

The hyperfine interaction with the axial amine nitrogen is expected to be very small and could not be observed in the CW ENDOR experiments. To determine this interaction, additional X-band HYSCORE experiments of [Cu(**1**)] in toluene and MBA were undertaken (Supporting Information, Figure S14). Two distinct peaks at ∼3.4 and 4.2) MHz were observed, centered around the ^{13}C Larmor frequency, and could thus stem from nearby ^{13}C nuclei in altered arrangement (as we proposed previously).[44] However, in principle, an appropriate combination of ^{14}N hyperfine and nuclear quadrupole couplings could also lead to double-quantum cross-peaks at this position. In order to test this, the HYSCORE spectrum of [Cu(**1**)] dissolved in pyridine (Py) was also recorded (Figure S14, Supporting Information). Analysis of the resulting spectra proved that the cross peaks observed for [Cu(**1**)] + MBA are indeed due to the weak interaction with the amine nitrogen. The simulated parameters are given in Table 3.

In summary, ENDOR and HYSCORE were employed to examine the structure of the bound asymmetric adducts via analysis and comparison of the spectra. Unfortunately, despite the fact that the ^{1}H ENDOR spectra of the imine protons did reveal a lowering in the symmetry of the adducts, the hyperfine data did not reveal any diastereomeric discrimination, as detected by EPR. The data did, however, confirm the weak binding mode of MBA to the Cu complexes (i.e., upon MBA binding the ligand ^{14}N couplings changed only slightly, the amine ^{1}H and ^{14}N couplings were very small, and the ligand methine and *tert*-butyl groups were hardly affected).

Table 2. ^{1}H Hyperfine Values Obtained by DFT Computations for the *R,R*-[Cu(1)] + *R*-MBA and *R,R*-[Cu(1)] + *S*-MBA Adducts Corresponding to the Optimized Structures A, B, and C (Figure 5)[a]

	DFT			experimental		
nuclei	A_1	A_2	A_3	A_1	A_2	A_3
imine protons						
[Cu(1)]				18.5	17.2	22.1
[Cu(2)]				18.4	17.7	22.45
[Cu(1)] + MBA				17.2	16.6	21.0
[Cu(2)] + MBA (H_A)				16.6	17.2	21.3
(H_B)				16.6	16.1	21.3
A H1 (imine)[b]	20.16	23.97	19.36			
H2 (imine)	28.54	24.58	23.85			
B H1 (imine)[b]	22.25	25.95	21.50			
H2 (imine)	27.49	23.60	22.90			
C H1 (imine)[b]	19.92	23.70	19.13			
H2 (imine)	28.83	24.85	24.08			
methine protons						
[Cu(1)]				−1.41	5.54	−1.43
A H1 (methine)[b]	−0.59	7.26	−1.67			
H2 (methine)	−0.05	5.77	−0.67			
B H1 (methine)[b]	0.03	7.50	−1.01			
H2 (methine)	−0.58	5.67	−1.51			
C H1 (methine)[b]	−0.89	6.91	−1.95			
H2 (methine)	−0.00	5.77	−0.71			
tert-butyl protons						
[Cu(1)]				−1.64	−1.50	3.30
A H (*tert*-butyl)	−1. 11	−1.41	2.81			
	−1.08	−1.47	3.16			
	−1.07	−1.50	3.91			
	−1.15	−1.40	2.97			
B H (*tert*-butyl)	−1.06	−1.29	2.70			
	−1.11	−1.59	3.14			
	−1.21	−1.67	2.34			
	−1.06	−1.31	2.68			
C H (*tert*-butyl)	−1.10	−1.37	2.96			
	−1.08	−1.49	3.15			
	−1.09	−1.51	2.89			
	−1.10	−1.39	2.79			
amine protons						
[Cu(1)]				−2.52	−4.87	3.62
[Cu(2)]				−2.62	−5.20	3.62
A H ($-NH_2$)	−4.08	−4.40	7.73			
H ($-NH_2$)	−3.34	−3.61	6.25			
B H ($-NH_2$)	−3.09	−2.88	5.03			
H ($-NH_2$)	−4.16	−4.51	7.94			
C H ($-NH_2$)	−2.60	−2.74	4.50			
H ($-NH_2$)	−3.95	−4.54	7.84			
A H (α_H MBA)	−1.27	−1.32	2.71			
B H (α_H MBA)	−1.88	−2.03	3.90			
C H (α_H MBA)	−2.27	−2.42	4.80			

[a] The experimental ^{1}H values obtained by ENDOR are also given. All *A* values given in MHz. [b] Nucleus on the same side of the complex as the MBA phenyl group; the hyperfine and quadrupole values were computed with the basis set EPR-II. Error in *A* values for H^{imine}, $H^{t\text{-}butyl}$, and $H^{methine}$ = ±0.02 MHz. Error in *A* values for H^{NH2} = ±0.05 MHz.

COMPUTATIONAL DFT ANALYSIS

The interaction of *R*- and *S*-MBA with *R,R*-[Cu(**1**)] was also studied computationally. The metal complex was studied at the QM (BHandH) level, while the aliphatic *tert*-butyl groups and cyclohexyl backbone were studied at the MM level (UFF). The Cu···N^{amine} distance was initially fixed at a relatively short 2.2 Å, and the bound MBA substrate was allowed to rotate about the Cu−N bond in 10° steps. The plot of the relative energy versus the O−Cu···N−C dihedral angle for *R,R*-[Cu(**1**)] with *R*-MBA is shown in the Supporting Information (Figure S16). Two clear energy minima were found for *RR* + *R* corresponding to

Table 3. Experimental (and Calculated) ^{14}N Hyperfine and Nuclear Quadrupole Values Obtained by ENDOR and HYSCORE[a]

nuclei	A_1[b]	A_2	A_3	P_1[c]	P_2	P_3	e^2qQ/h[g]	η[h]
[Cu(**1**)][I]	50.5	37.4	38.5	−1.15	0.70	0.45	−2.3	0.2
[Cu(**2**)][I]	50.4	36.6	38.0	−1.25	0.64	0.48	−2.5	0.15
[Cu(**1**)] + MBA	49.7	35.9	36.4	−1.20	0.70	0.50	−2.4	0.2
[Cu(**2**)] + MBA	50.0	34.2	38.0	−1.25	0.80	0.45	−2.5	0.0
N (MBA)[d]	0.7[e]	0.8[e]	0.9[f]				3.3	0.9
A N1*	34.37	48.05	35.79	1.01	−1.25	0.24		
N2	52.92	36.74	38.35	−1.30	1.02	0.28		
B N1*	34.90	49.83	36.60	1.00	−1.30	0.30		
N2	51.43	35.43	37.35	−1.35	1.02	0.33		
C N1*	33.62	47.12	35.06	1.01	−1.28	0.27		
N2	53.40	37.65	38.65	−1.29	1.02	0.27		
A N (MBA)	−0.81	−0.85	0.29	1.29	0.93	−2.22		
B N (MBA)	−0.75	−0.77	0.37	1.29	0.91	−2.20		
C N (MBA)	−0.77	−0.78	0.39	1.29	0.89	−2.18		

[a] The corresponding ^{14}N values obtained by DFT computations for the *R,R*-[Cu(**1**)] + *R*-MBA and *R,R*-[Cu(**1**)] + *S*-MBA adducts are also given, corresponding to the optimized structures labeled **A**, **B**, and **C** (Figure 5). All *A* and *P* values given in MHz. [b] *A* values ±0.2 MHz. [c] *P* values ±0.1 MHz. [d] Euler angles = [30 13 0]° ± 10°. [e] ±0.1 MHz. [f] ±0.3 MHz. [g] ±0.2 MHz. [h] ±0.1 MHz. [I] Only the values for N2 are given. Those for N1 are identical; both ***A*** and ***P*** tensors are rotated in a plane 90° around the $\boldsymbol{A}_3$ ($\boldsymbol{P}_3$) axis.

dihedral angles of $\varphi = -102°$ and 139° (definition of this angle is given in the Supporting Information, Figure S15) with one minimum for *RR* + *S* possessing a dihedral angle of $\varphi = -21.9°$. Free optimization of the energy at these minima was then allowed, which resulted in slightly longer Cu···N^{amine} distances of 2.255 and 2.253 Å for the *RR* + *R* adducts and 2.267 Å for the *RR* + *S* adduct. These structures are hereafter labeled **A**, **B**, and **C** respectively (Figure 5). Structures **A** and **B** were practically isoenergetic (although there was a 2 kJ mol^{-1} difference between the two in favor of **A**), while both were at least 7 kJmol^{-1} lower in energy than all other *RR* + *R* orientations. Most importantly, structure **C** for the heterochiral *RR* + *S* was found to be 5 kJ mol^{-1} lower in energy compared to the homochiral adducts *RR* + *R*. Note that unrestricted optimization of the *RR* + *S* adduct led to a final structure **C** with the MBA phenyl orientation quite similar to the one obtained for the most stable structure **A** of the *RR* + *R* adduct (Figure 5).

Although the inability of DFT to accurately quantify dispersion effects renders it unsuitable for modeling $\pi-\pi$ interactions, the computational results indicate that the adduct could be likely stabilized by an offset $\pi-\pi$ interaction between the phenyl ring of MBA and the imine group of the complex. This is in keeping with the $\pi-\pi$ rules outlined by Hunter and Sanders[22a] and could explain the lower symmetry of the adducts observed by EPR and ENDOR. Recent work on benzene, pyridine, and DNA base dimers demonstrated minima on the potential energy surfaces with the BHandH functional.[34] They attributed this ability to qualitatively reproduce geometric details to a fortuitous cancellation of errors within the functional and demonstrated that it applied to a range of $\pi-\pi$ interacting systems, reproducing energies generally to within ±2 kJ mol^{-1} of the MP2 values. For these reasons this functional was used here with the BHandH to model the $\pi-\pi$ interactions. However, no improvements were observed in the calculations of the structures **A**, **B**, and **C**, so we did not consider further the stabilization role of $\pi-\pi$ interactions in our interpretations.

In a next step, the spin Hamiltonian parameters were computed for the three optimized DFT structures **A**, **B**, and **C**. The relevant EPR parameters are presented in Tables 1−3. Despite the fact that current state-of-the-art DFT methods still struggle to exactly reproduce the *g* and metal hyperfine values of metal complexes,[45] the agreement between experimental g/A^{Cu} values and the calculated parameters (Table 1) is satisfactory. The in-plane principal ***g*** and $^{Cu}\boldsymbol{A}$ tensor axes

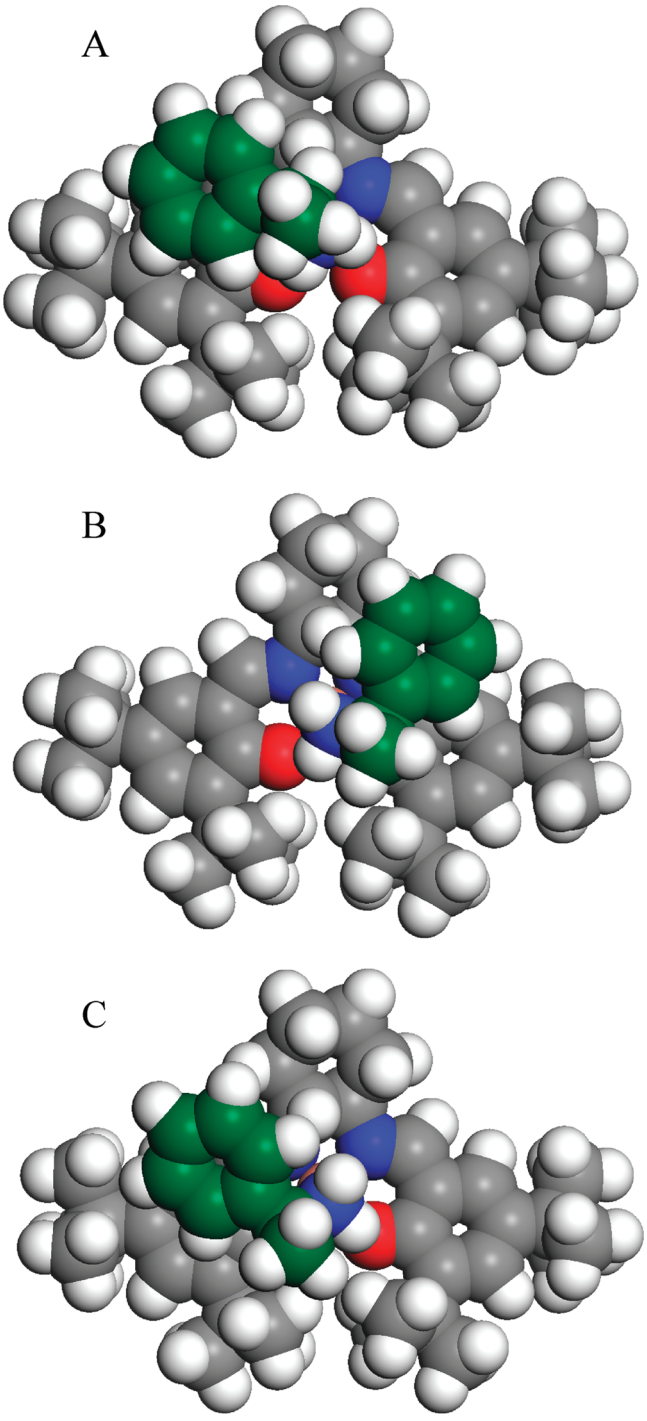

Figure 5. QMMM-optimized structures for *R*-MBA with *R,R*-[Cu(**1**)] from the constrained scan reported in Figure S14, Supporting Information, giving structure **A** (Cu···*N* = 2.255 Å) and structure **B** (Cu···*N* = 2.253 Å). Structure **C** is optimized from the equivalent scan for *S*-MBA with *R,R*-[Cu(**1**)], giving Cu···*N* = 2.267 Å. Atom colors: for clarity, C ([Cu(**1**)]) and C(MBA) are colored gray and green, respectively; N, blue; O, red; H, white; Cu, pink.

dx.doi.org/10.1021/ic200113u |*Inorg. Chem.* 2011, 50, 6944–6955

were found to be colinear, pointing approximately along the O−Cu−N axes. The calculated ligand ^{14}N hyperfine and quadrupole parameters are listed in Table 3. The ligand (**1**) nitrogens, labeled N1 and N2, were found to be inequivalent in terms of their hyperfine and nuclear quadrupole parameters. N1 refers to the ligand ^{14}N nucleus under the phenyl ring of the bound MBA substrate (i.e., on the same side of the [Cu(**1**)] complex; see Figure 5), while N2 refers to the ^{14}N nucleus on the opposite side of the complex from the MBA. The N1 and N2 hyperfine and nuclear quadrupole tensors are approximately colinear with the ***g*** tensor axes, with the largest hyperfine value lying along the Cu−N axes. The agreement between experimental data and theory (Table 3) is very good. Interestingly, while slight inequivalencies between the two ligand ^{14}N nuclei revealed via DFT, these difference were not directly observed experimentally (although a slight broadening of the peaks was indeed detected in the ^{14}N ENDOR spectra, suggestive of in-equivalent ^{14}N nuclei; Supporting Information). The *A* and *P* parameters for the ^{14}N nucleus of the weakly interacting MBA substrate were detected via X-band HYSCORE, and the results are also in reasonable agreement with the computed values (Table 3).

The slight lowering in the symmetry of the adduct upon MBA coordination was detected experimentally via the inequivalency of the resulting *A* values for $H_{A,B}^{imine}$ (Figure 4 and Table 2). This was also confirmed in the computed *A* values for both the imine and the methine protons. For example, in structure **A**, two sets of *A* values for $H_{A,B}^{imine}$ were calculated (Table 2). The computed *A* values for $H^{methine}$ were also found to be inequivalent; this was not be detected experimentally and is possibly due to a slight distribution in the conformations. Nevertheless, the agreement between the experimental and calculated *A* values for H^{imine} and $H^{methine}$ are very good. A range of *A* values was extracted from the computational studies for the inner *tert*-butyl groups, since the absolute values obtained depended on the adopted rotational conformation. The hyperfine values for the four closest $H^{t\text{-butyl}}$ protons are listed in Table 2, while all the remaining protons produced smaller *A* values. The experimental values represent an excellent average of the four closest $H^{t\text{-butyl}}$ hyperfine values listed in Table 2.

According to the calculations, two distinct sets of hyperfine values were found for protons originating from the bound MBA substrate; these included the amine $-NH_2$ protons and the α-proton attached to the asymmetric carbon atom of MBA (Scheme 1). For example, the calculated *A* values for the $-NH_2$ protons for structure **A** are somewhat different from the experimental values (Table 2). This is not surprising since these hyperfine values will be very sensitive to small changes in the MBA ligand orientation and the Cu−N^{MBA} distance. Again, the calculated asymmetry of the NH_2 protons was not observed in the experiment, in part due to a possible distribution of conformers and also due to the broader line widths for these protons in the ENDOR spectra. A smaller α-proton hyperfine was also calculated (Table 2), although this hyperfine was not observed in the experimental ENDOR spectra, as the peaks would be superimposed on other ligand-derived peaks, making any useful assignment very difficult.

DISCUSSION

Stereoselective Binding of MBA with [Cu(1,2)]. In previous studies, we investigated the discrimination of chiral epoxides[20] by chiral [VO(**1**)] complexes. The [VO(**1**)] + epoxide adducts were very weak, but differences in the EPR and ENDOR spectra of the homochiral and heterochiral adducts were readily identifiable.[20] The origin of this enantioselectivity was based upon a series of weak H bonds, augmented by an electrostatic interaction, between the epoxide substrate and the [VO(**1**)] ligand. Crucially these hydrogen bonds facilitated the overall orientation of the epoxide between the metal center and the chiral salen backbone.[20]

In the present system, differences in diastereomeric adducts were sufficiently pronounced that enantiomer discrimination was directly manifested in the W-band EPR spectra. The heterochiral Cu−MBA combinations (*RR*-*S* and *SS*-*R*) were found to be the preferred adducts with selectivities of 86 ± 5% and 57 ± 5% for [Cu(**1**)] and [Cu(**2**)], respectively. While the role of H bonds was shown to be instrumental in controlling the stereoselectivities of the [VO(**1**)]−epoxides system,[20] the mode of stereochemical communication between [Cu(**1**,**2**)] and *R*-/*S*-MBA must also be rationalized.

According to the computational DFT results for the homochiral (*R*,*R*-[Cu(**1**)] + *R*-MBA) and heterochiral (*R*,*R*-[Cu(**1**)] + *S*-MBA) adducts, the bulky MBA substrate was found to bind to the bulky [Cu(**1**)] complex. The heterochiral adduct was energetically favored (by only 5 kJ mol^{-1}) in agreement with the experimental observation. Two discrete energy minima were identified in the homochiral adducts (structures **A** and **B**; Figure 5) in which the MBA-phenyl group was positioned over either phenyl ring of ligand (**1**). In the heterochiral adduct (structure **C**; Figure 5) a slightly different alignment of the MBA-phenyl ring was observed. Nevertheless, in all cases, the adducts were found to be less energetically preferred when the MBA-phenyl ring was positioned over the *tert*-butyl groups in [Cu(**1**)] due to steric hindrance. Furthermore, the methyl group attached to the asymmetric carbon atom of MBA was always found to point 'upward' and away from the ligand plane in all adducts (Figure 5). As a result, the single α-proton attached to this same asymmetric carbon atom of MBA points 'downward' toward the ligand. This has important consequences for controlling the stereoselective binding in homo- vs heteroadducts as discussed below.

In structure **A**, the closest contact points of MBA with [Cu(**1**)] (apart from the Cu···N^{amine} contact) was between the methine ligand proton and both the α-proton and *o*-phenyl proton of MBA ($H^{methine}$···$H^{\alpha\text{ or ortho}}$ distances of 2.40 and 2.58 Å respectively). In this homochiral adduct, the arrangement is such that the α-proton of *R*-MBA points *toward* the methine proton in *R*,*R*-[Cu(**1**)] (Figure 5A). However, in the heterochiral adduct, this α-proton of *S*-MBA points *away* from the methine proton in *R*,*R*-[Cu(**1**)] (Figure 5C). As a result, the closest point of contact with *S*-MBA is now only between the methine ligand proton and the *o*-phenyl proton of MBA (distance of 2.47 Å). This slight difference in steric crowding caused by the α-proton of MBA appears to be sufficient to tip the balance of selectivity in favor of the heterochiral adduct.

It should also be mentioned that although there was little difference in energy between structures **A** and **B** (for the homochiral adduct), close inspection of the structures reveals that the MBA-phenyl ring is slightly displaced over the cyclohexyl ring of (**1**) in structure **B**. As a result, more of the MBA-phenyl ring protons now overlap the staggered cyclohexyl ring protons, and this creates a small but unfavorable amount of steric crowding. Such an outcome is not observed in structure **A**, where only two points of closest contact are observed (see above). This may be responsible for the slight preference for the amine to bind on one side of the complex in *R*,*R*-[Cu(**1**)] + *R* (structure **A**).

It is important to emphasize that the MBA substrate is effectively trapped in one of two positions when bound to [Cu(**1**)], for example, on one side of the chiral salen complex as shown in Figure 5 (**A** or **B**). This is due to the inability of the MBA-phenyl ring to easily pass over the cyclohexyl ring due to the axial methine proton, which is virtually perpendicular to the

salen ligand plane. This methine proton, on the asymmetric carbon center of the diamine backbone, thus creates a barrier to MBA rotation. While this ligand proton is not directly involved in the stereoselectivity for MBA binding (as occurs for chiral discrimination via H bonds in [VO(**1**)] + epoxides),[20] it does indirectly influence the mode of binding by restricting easy movement of the substrate from structure **A** to **B**. Furthermore, due to steric interactions with the α-proton attached to the asymmetric carbon atom of *R*-MBA, this methine proton is also indirectly responsible for favoring the heterochiral structure **C** over the homochiral structure **A**.

Finally, removal of the *tert*-butyl groups in [Cu(**2**)] enables the chiral MBA substrates to adopt more binding orientations relative to [Cu(**1**)]. In particular, the MBA substrate does not experience any steric repulsion caused by the bulky ligand groups in [Cu(**1**)]; as more orientations are accessible, the stereoselectivity in the binding obviously decreases substantially to only 57 ± 5%. Despite the fact that the MBA-phenyl ring can potentially overlap and π stack with the ligand phenyl rings (Figure 5) and thus facilitate further stabilization of the adducts, DFT was unable to accurately quantify these possible contributions.

Implications of Findings for Asymmetric Homogeneous Catalysis. One of the unique features of privileged chiral catalysts is their ability to deliver a broad applicability for so many diverse reactions. Clearly certain key structural features of the catalysts are important to achieve these high levels of enantioselectivities. Bulky framework substituent's are known to prevent stabilization of transition states, particularly in asymmetric catalysis, since the transition states for the two diastereomers have similar energies (although one will have a slightly lower kinetic barrier compared to the other). This is particularly true in chiral metal salen complexes, whereby the enantioselectivities of the asymmetric epoxidation reactions using the Mn(salen) catalyst depends on the bulky substituents at the 3,3′ and 5,5′ positions.[9c,46] These bulky substituents not only prevent stabilization of transition states but also play another important role by blocking and regulating the orientation of the incoming substrates, creating a high diastereofacial preference.[9c,46]

It is clear from the results presented here that strong diastereomeric discrimination of one specific enantiomer of a substrate occurs in the *R,R*-[Cu(**1**)] complex (86 ± 5% for *RR-S* and *SS-R*). In the absence of these bulky substituents (as in [Cu(**2**)]) the diastereomeric discrimination of the chiral amine substrates is substantially reduced (57 ± 5% for *RR-S* and *SS-R*). This indicates that the *tert*-butyl groups are directly implicated in regulating chiral recognition and can help in the differentiation between different stereoisomers of the amine. As the DFT results have shown, subtle steric hindrance between substrate substituents (such as MBA α-proton) and ligand substituents (such as *tert*-butyl or $H^{methine}$) are responsible for destabilizing one diastereomeric adduct in favor of another. While the presence of such diastereomeric adducts are often presumed as mechanistic intermediates, they are rarely observed directly in cases of weak complex−substrate interactions. The results reported here therefore demonstrate the useful role of W-band EPR in probing such diastereomeric adducts which may be of direct relevance to studies in homogeneous asymmetric catalysis.

CONCLUSIONS

The asymmetric interaction of the chiral amines (*R-*/*S*-methylbenzylamine) with the chiral [Cu(**1,2**)] complexes was revealed by CW EPR and DFT. The spectroscopic data revealed that only one MBA substrate bound weakly to the copper complexes. Diastereomeric discrimination of MBA enantiomers was directly observed by W-band EPR, revealing an 86:14 preference for the heterochiral adducts (*RR-S* and *SS-R*) in [Cu(**1**)]; this diminished to 57:43 in favor of the heterochiral adducts in [Cu(**2**)]. The symmetry of the [Cu(**1,2**)] + MBA adducts was lowered compared to the uncoordinated [Cu(**1,2**)] complexes; as reflected in the rhombic *g* distortions, this lower symmetry resulted from the preferential binding and orientation of the MBA substrate onto one side of the chiral Cu complex.

While the W-band EPR data revealed the selectivity of MBA binding, the origin of this selectivity was explained by DFT. The results revealed that the bulky phenyl ring of MBA destabilized formation of any adduct which placed the MBA-phenyl ring over the *tert*-butyl groups at positions 3,3′ and 5,5′ of the complex. Instead, steric hindrance between the complex and the substrate was minimized when the MBA-phenyl ring was positioned over the phenyl rings of the [Cu(**1**)] complex. Two stabilization sites were identified in the homochiral adduct *R,R*-[Cu(**1**)] + *R*-MBA (labeled **A** and **B**); structure **A** was slightly preferred by 2 kJ mol^{-1} due to the small unfavorable steric interactions between the MBA-phenyl ring and the ligand cyclohexyl ring that occurred in **B**. However, the most stable site was found for the heterochiral adduct *R,R*-[Cu(**1**)] + *S*-MBA (labeled **C**), in agreement with the experiments. This site **C** was slightly preferred by 5 kJ mol^{-1} compared to the homochiral adduct sites **A** and **B**. In this heterochiral case, the α-proton of *S*-MBA was found to point away from the ligand methine proton; the reverse situation occurred in the homochiral adducts. These results reveal how very weak, and indeed subtle, outer-sphere interactions are responsible for controlling stereoselective binding in chiral complex−chiral substrate interactions.

ASSOCIATED CONTENT

Supporting Information. Further experimental details, X-band EPR spectra of [Cu(**2**)] in MBA, determination of the coordination number of MBA molecules, supporting ^{1}H and ^{14}N CW and pulsed ENDOR spectra, HYSCORE, and additional DFT details. This material is available free of charge via the Internet at http://pubs.acs.org.

AUTHOR INFORMATION

Corresponding Author

*E-mail: MurphyDM@cardiff.ac.uk; sabine.vandoorslaer@ua.ac.be.

ACKNOWLEDGMENT

This work was supported by EPSRC funding (EP/E030122), by the Hercules Foundation, Flanders (contract AUHA013), and a NOI-BOF grant of the University of Antwerp (to S.V.D.).

REFERENCES

(1) (a) Heitbaum, M.; Glorius, F.; Escher, I. *Angew. Chem., Int. Ed.* **2006**, *45*, 4732–4762. (b) Jacobsen, E. N., Pfaltz, A., Yamamoto, H., Eds.; In *Comprehensive Asymmetric Catalysis*; Springer: New York, 1999; Vols. 1−3. (c) Ojima, I., Ed.; In *Catalytic Asymmetric Synthesis*, 2nd ed.; Wiley-VCH: New York, 2000.

(2) (a) Noyori, R. *Angew. Chem., Int. Ed.* **2002**, *41*, 2008–2022. (b) Knowles, W. S. *Angew. Chem., Int. Ed.* **2002**, *41*, 1998–2007. (c) Sharples, K. B. *Angew. Chem., Int. Ed.* **2002**, *41*, 2024–2032.

(3) (a) Walsh, P. J.; Kozlowski, M. C. *Fundamentals of asymmetric catalysis*; University Science Books: Sausalito, CA, 2009. (b) In *Asymmetric synthesis—The essentials*, 2nd ed.; Christmann, M., Brase, S., Eds.; Wiley-VCH: New York, 2008.

(4) Yoon, T. P.; Jacobsen, E. M. *Science* **2003**, *299*, 1691–1693.

(5) (a) Jacobsen, E. N. In *Catalytic Asymmetric Synthesis*; Ojima, I., Ed.; VCH: Weinheim, 1993. (b) Jacobsen, E. N. In *Comprehensive Organometallic Chemistry II*; Wilkinson, G.; Stone, F.G.A.; Abel, E. W., Hegedus, L. S., Eds.; Pergamon Press, New York, 1995; Vol. 12. (c) Katsuki, T. *Coor. Chem. Rev.* **1995**, *140*, 189–214. (d) Dalton, C. T.; Ryan, K. M.; Wall, V. M.; Bousquet, C.; Gilheany, D. G. *Top. Catal.* **1998**, *5*, 75. (e) Canalai, L.; Sherrington, D. C. *Chem. Soc. Rev.* **1999**, *28*, 85–93.

(6) (a) Costas, M.; Mehn, M. P.; Jensen, M. P.; Que, L., Jr. *Chem. Rev.* **2004**, *104*, 939–986. (b) Di Mauro, E. F.; Mamai, A.; Kozlowski, M. C. *Organometallics* **2003**, *22*, 850–855.

(7) (a) Collman, J. P.; Zhang, A.; Lee, V. J.; Uffelman, E. S.; Brauman, J. I. *Science* **1993**, *261*, 1404–1411. (b) Sono, M.; Roach, M. P.; Coulter, E. D.; Dawson, J. H. *Chem. Rev.* **1996**, *96*, 2841–2888.

(8) Venkataramanan, N. S.; Kuppuraj, G.; Rajagopal, S. *Coord. Chem. Rev.* **2005**, *249*, 1249–1268.

(9) (a) Katsuki, T. *Adv. Synth. Catal.* **2002**, *344*, 131–147. (b) Katsuki, T. *Curr. Chem. Org.* **2001**, 63. (c) Palucki, M.; Finney, N. S.; Pospisil, P. J.; Guler, M. L.; Ishida, T.; Jacobsen, E. N. *J. Am. Chem. Soc.* **1998**, *120*, 948–954. (d) Tokunaga, M.; Larrow, J. F.; Kakiuchi, F.; Jacobsen, E. N. *Science* **1997**, *277*, 936–938.

(10) Jacobsen, E. N. *Acc. Chem. Res.* **2000**, *33*, 421–431.

(11) (a) Fraile, J. M.; Garcia, J. I.; Jimenez-Oses, G.; Mayoral, J. A.; Roldan, M. *Organometallics* **2008**, *27*, 2246–2251. (b) Di Tommaso, D.; French, S. A.; Zanotti-Gerosa, A.; Hancock, F.; Palin, E. J.; Catlow, C. R. A. *Inorg. Chem.* **2008**, *47*, 2674–2687. (c) Ihori, Y.; Yamashita, Y.; Ishitani, H.; Kobayashi, S. *J. Am. Chem. Soc.* **2005**, *44*, 15528–15535. (d) Brandt, P.; Södergren, M. J.; Gandersson, P.; Norrby, P.-O. *J. Am. Chem. Soc.* **2000**, *122*, 8013–8020.

(12) (a) Van Doorslaer, S.; Caretti Giangaspro, I.; Fallis, I. A.; Murphy, D. M. *Coor. Chem. Rev.* **2009**, *253*, 2116–2130. (b) Carter, E.; Murphy, D. M. In *Spectroscopic Properties of Inorganic and Organometallic Compounds*; Douthwaite, R., Duckett, S., Eds.; RSC: Cambridge, 2009; Vol. 4, pp 355−384.

(13) (a) Bolm, C.; Martin, M.; Gescheidt, G.; Palivan, C.; Stanoeva, T.; Bertagnolli, H.; Feth, M.; Schweiger, A.; Mitrikas, G.; Harmer, J. *Chem.—Eur. J.* **2007**, *13*, 1842–1850. (b) Bolm, C.; Martin, M.; Gescheidt, G.; Palivan, C.; Neshchadin, D.; Bertagnolli, H.; Feth, M.; Schweiger, A.; Mitrikas, G.; Harmer, J. *J. Am. Chem. Soc.* **2003**, *125*, 6222–6227.

(14) Srinivasan, K.; Michaud, P.; Kochi, K. J. *J. Am. Chem. Soc.* **1986**, *108*, 2309–2320.

(15) (a) Bryliakov, K. P.; Babushkin, D. E.; Talsi, E. P. *J. Mol. Catal. A* **2000**, *158*, 19–35. (b) Bryliakov, K. P.; Khavrutskii, I. V.; Talsi, E. P.; Kholdeeva, O. A. *React. Kinet. Catal. Lett.* **2000**, *71*, 183–191. (c) Bryliakov, K. P.; Kholdeeva, O. A.; Vanina, M. P.; Talsi, E. P. *J. Mol. Catal. A* **2002**, *178*, 47–53.

(16) Campbell, K. A.; Lashley, M. R.; Wyatt, J. K.; Nantz, M. H.; Britt, R. D. *J. Am. Chem. Soc.* **2001**, *123*, 5710–5719.

(17) Hsieh, W.-Y.; Pecoraro, V. L. *Inorg. Chim. Acta* **2002**, *341*, 113–117.

(18) (a) Bryliakov, K. P.; Lobanova, M. V.; Talsi, E. P. *J. Chem. Soc., Dalton Trans.* **2002**, 2263–2265. (b) Bryliakov, K. P.; Talsi, E. P. *Inorg. Chem.* **2003**, *42*, 7258–7265.

(19) (a) Vinck, E.; Murphy, D. M.; Fallis, I. A.; Strevens, R. R.; Van Doorslaer, S. *Inorg. Chem.* **2010**, *49*, 2083–2092. (b) Vinck, E.; Van Doorslaer, S.; Murphy, D. M.; Fallis, I. A. *Chem. Phys. Lett.* **2008**, *464*, 31–37. (c) Vinck, E.; Murphy, D. M.; Fallis, I. A.; Van Doorslaer, S. *Appl. Magn, Reson.* **2010**, *37*, 289–303.

(20) Movassaghi, M.; Jacobsen, E. M. *Science* **2002**, *298*, 1904–1905.

(21) (a) Fallis, I. A.; Murphy, D. M.; Willock, D. J.; Tucker, R. J.; Farley, R. D.; Jenkins, R.; Strevens, R. *J. Am. Chem. Soc.* **2004**, *126*, 15660–15661. (b) Murphy, D. M.; Fallis, I. A.; Landon, J.; Willock, D. J.; Carter, E.; Van Doorslaer, S.; Vinck, E. *Phys. Chem. Chem. Phys.* **2009**, *11*, 6757–6769. (c) Murphy, D. M.; Fallis, I. A.; Willock, D. J.; Landon, J.; Carter, E.; Vincks, E. *Angew. Chem., Int. Ed.* **2008**, *47*, 1414–1416. (d) Carter, E.; Murphy, D. M.; Fallis, I. A.; Willock, D. J.; Van Doorslaer, S.; Vinck, E. *Chem. Phys. Lett.* **2010**, *486*, 74–79.

(22) (a) Hunter, C. A.; Sander, J. K. M. *J. Am. Chem. Soc.* **1990**, *112*, 5525–5534. (b) Miyamura, K.; Mihara, A.; Fujii, T.; Gohshi, Y.; Ishii, Y. *J. Am. Chem. Soc.* **1995**, *117*, 2371–2318. (c) Askew, B.; Ballester, P.; Buhr, C.; Jeong, K. S.; Jones, S.; Parris, K.; Williams, K.; Rebek, J. *J. Am. Chem. Soc.* **1989**, *111*, 1082–1090. (d) Abraham, R. J.; Eivazi, F.; Pearson, H.; Smith, K. M. *J. Chem. Soc., Chem. Commum.* **1976**, 699–701. (e) Clever, G. H.; Carell, T. *Angew. Chem., Int. Ed.* **2007**, *46*, 250–253.

(23) (a) Lyubenova, S.; Maly, T.; Zwicker, K.; Brandt, U.; Ludwig, B.; Prisner, T. *Acc. Chem. Res.* **2010**, *43*, 181–189. (b) Goldfarb, D.; Arieli, D. *Ann. Rev. Biophys. Biomol. Struct.* **2004**, *33*, 441–468. (c) Astashkin, A. V.; Raitsimring, A. M.; Walker, F. A.; Rensing, C.; McEvoy, M. M. *J. Biol. Inorg. Chem.* **2005**, *10*, 221–230. (d) Derose, V. J.; Hoffman, B. M. *Methods Enzymol.* **1995**, *246*, 554–589. (e) Ames, W. M.; Larsen, S. C. *J. Biol. Inorg. Chem.* **2009**, *14*, 547–557.

(24) (a) Yoon, J.; Solomon, E. I. *Coor. Chem. Rev.* **2007**, *251*, 379–400. (b) Finazzo, C.; Calle, C.; Stoll, S.; Van Doorslaer, S.; Schweiger, A. *Phys. Chem. Chem. Phys.* **2006**, *8*, 1942–1953. (c) Wagner, M. R.; Walker, F. A. *Inorg. Chem.* **1983**, *22*, 3021–3028. (d) Shao, J. L.; Steene, E.; Hoffman, B. M.; Ghosh, A. *Eur. J. Inorg. Chem.* **2005**, *8*, 1609–1615. (e) Zhao, M.; Stern, C.; Barrett, A. G. M.; Hoffman, B. M. *Angew. Chem.* **2003**, *42*, 462–465.

(25) (a) Bunce, S.; Cross, R. J.; Farrugia, L. J.; Kunchandy, S.; Meason, L. L.; Muir, K. W.; Donnell, M. O; Peacock, R. D.; Stirling, D.; Teat, S. J. *Polyhedron* **1998**, *17*, 4179–4187. (b) Bernardo, K.; Leppard, S.; Robert, A.; Commenges, G.; Dahan, F.; Meunier, B. *Inorg. Chem.* **1996**, *35*, 387–396.

(26) Stoll, S.; Schweiger, A. *J. Magn. Reson.* **2006**, *178*, 42–55.

(27) Höfer, P.; Grupp, A.; Nebenführ, H.; Mehring, M. *Chem. Phys. Lett.* **1986**, *132*, 279–282.

(28) Madi, Z. L.; Van Doorslaer, S.; Schweiger, A. *J. Magn. Reson.* **2002**, *154*, 181–191.

(29) Davies, E. R. *Phys. Lett. A* **1974**, *A 47*, 1–2.

(30) (a) Schosseler, P.; Wacker, T.; Schweiger, A. *Chem. Phys. Lett.* **1994**, *224*, 319–324. (b) Schweiger, A.; Jeschke, G. *Principles of Pulse Electron Paramagnetic Resonance*; Oxford University Press: Oxford, 2001.

(31) Vreven, T.; Morokuma, K. *J. Comput. Chem.* **2000**, *21*, 1419–1432.

(32) Frisch, M. J.; et al. *Gaussian 03*, Revision C.02; Gaussian, Inc.: Wallingford, CT, 2004.

(33) Rappé, A. K.; Casewit, C. J.; Colwell, K. S.; Goddard, W. A., III; Skiff, W. M. *J. Am. Chem. Soc.* **1992**, *114*, 10024–10035.

(34) Waller, M. P.; Robertazzi, A.; Platts, J. A.; Hibbs, D. E.; Williams, P. A. *J. Comput. Chem.* **2006**, *27*, 491–504.

(35) Lee, C.; Yang, W.; Parr, R. G. *Phys. Rev. B* **1988**, *37*, 785–789.

(36) (a) Neese, F. *J. Chem. Phys.* **2001**, *115*, 11080–11096. (b) Neese, F. *J. Phys. Chem. A* **2001**, *105*, 4290–4299. (c) Neese, F. *J. Chem. Phys.* **2003**, *118*, 3939–3948. (d) Neese, F. *J. Chem. Phys.* **2005**, *122*, 34107(1)–34107(13).

(37) This basis is based on the TurboMole DZ basis developed by Ahlrichs and co-workers and obtained from the basis set library under ftp.chemie.unikarlsruhe.de/pub/basen. Unpublished results by R. Ahlrichs and co-workers.

(38) Barone, V. In *Recent Advances in Density Functional Methods*; Chong, D. P., Ed.; World Scientific Publ. Co.: Singapore, 1996; p 287.

(39) (a) Schaefer, A.; Horn, H.; Ahlrichs, R. *J. Chem. Phys.* **1992**, *97*, 2571–2577. (b) The Ahlrichs (2df,2pd) polarization functions were obtained from the TurboMole basis set library under ftp.chemie.uni-karlsruhe.de/pub/basen. Unpublished results by R. Ahlrichs and co-workers.

(40) Sinnecker, S.; Rajendran, A.; Klamt, A.; Diedenhof, M.; Neese, F. *J. Phys. Chem. A* **2006**, *110*, 2235–2245.

(41) (a) Schweiger, A. *Struct. Bonding (Berlin)* **1982**, *51*, 1. (b) Hs., H.; Günthard, A.; Schweiger *Chem. Phys.* **1978**, *32*, 35–61. (c) Pilbow, J. R. *Transition Ion Electron Paramagnetic Resonance*; Oxford Science Publications: Oxford, 1990.

(42) Kita, S.; Hashimoto, M.; Iwaizumi, M. *Inorg. Chem.* **1979**, *18*, 3432–3438.

(43) (a) Pratt, R. C.; Stack, T. D. P. *J. Am. Chem. Soc.* **2003**, *12*, 8716–8717. (b) Pratt, R. C.; Mirica, L. M.; Stack, T. D. P. *Inorg. Chem.* **2004**, *43*, 8030–8039. (c) Pratt, R. C.; Stack, T. D. P. *Inorg. Chem.* **2005**, *44*, 2367–2375.

(44) Van Doorslaer, S.; Murphy, D. M.; Fallis, I. A. *Res. Chem. Intermed.* **2007**, *33*, 807–823.

(45) (a) Waller, M. P.; Robertazzi, A.; Platts, J. A.; Hibbs, D. E.; Williams, P. A. *J. Comput. Chem.* **2006**, *27*, 491–504. (b) Neese, F. *J. Biol. Inorg. Chem.* **2006**, *11*, 702–711. (c) Neese, F.; Munzarova, M. L. In *Calculation of NMR and EPR parameters*; Kaupp, M., Buhl, M., Malkin, V. G., Eds.; Wiley-VCH: Weinheim, 2004; p 21. (d) Stein, M.; van Lenthe, E.; Baerends, E. J.; Lubitz, W. *J. Am. Chem. Soc.* **2001**, *123*, 5839–5840. (e) Neese, F. *Coord. Chem. Rev.* **2009**, *256*, 526–563.

(46) (a) Zhang, W.; Loebach, J. L.; Wilson, S. R.; Jacobsen, E. N. *J. Am. Chem. Soc.* **1990**, *112*, 2801–2803. (b) McGarrigle, E. M.; Gilheany, D. G. *Chem. Rev.* **2005**, *105*, 1563–1602.